Contents lists available at ScienceDirect

Journal of Solid State Chemistry

An X-ray diffraction, magnetic susceptibility and spectroscopic studies of $Yb_{2-x}Cr_xO_3$

S. Hamdi [a], M. Amami [a], E.K. Hlil [b], R. Ben Hassen [a,*]

[a] Unité de Recherche de Chimie des Matériaux, ISSBAT, Université Tunis ElManar, 9 Avenue Dr. Zouhaier Safi, 1006 Tunis, Tunisia
[b] Institut Néel CNRS, Département MCMF, B.P. 166, 38042 Grenoble Cedex 9, France

ARTICLE INFO

ABSTRACT

Polycrystalline samples with general formula $Yb_{2-x}Cr_xO_3$ ($0 < x < 0.03$), obtained by sol–gel method and analyzed by X-ray diffraction, formed solid solutions over all the mentioned range. Cr showed a maximum solubility of 2.8 mol% in Yb_2O_3 sesquioxide at 1000 °C. A preferential substitution of Cr^{3+} ions over two cationic sites, $8b$ and $24d$ in the space group Ia-3 was found. The lattice parameters a are found to vary linearly (10.4402(4) Å $< a < $ 10.4372(1) Å) with the composition x. The two independent atoms Yb/Cr have octahedral coordination; however, the degrees of distortion of their coordination polyhedron are different. Replacing Yb^{3+} by Cr^{3+} introduces slight changes in the atomic coordinates leading to an increase of the mean cation-anion distances. The ability of Raman spectroscopy to detect changes in local coordination is utilized. A pseudo-tetrahedral coordination for the Cr^{3+} in the $24d$ site was found. Magnetic susceptibility measurements of all samples were done in a temperature range of 2–50 K. For $T < 37$ K, the inverse paramagnetic susceptibilities depend linearly on temperature. However, in the high-temperature region, for $T > 37$ K, the inverse paramagnetic susceptibilities are non-linear versus temperature. This deviation from the Curie–Weiss behaviour was discussed.

1. Introduction

Rare-earth sesquioxides (R_2O_3, $R=$lanthanide, Y or Sc) possess unique physical and chemical properties, which make them technologically very important and many review articles dealing with fundamentals and applications of these materials have already been published [1,2]. Y_2O_3 and Yb_2O_3 have similar applications and properties. For example, both compounds are dopants commonly used to stabilize ZrO_2 ceramic films, which are widely used as thermal barrier coatings (TBCs). Ytterbium oxide is also an additive used to self-reinforce silicon nitride ceramics [3]. Ytterbium-doped YAG is one of the most promising laser-active materials and is more suitable for diode-pumping than the traditional Nd-doped crystals. Highly ytterbium-doped YAG thin films also show promise for various laser waveguide applications in photonic devices.

The crystallographic data and polymorphism of the rare-earth sesquioxides were first reviewed by Brauer [4] and updated by Haire and Eyring [5]. Depending on the temperature and the radius of R^{+3}-cation rare-earth sesquioxides are known to occur in five polymorphic modifications, A-, B-, C-, H-, and X-R_2O_3. In the C-type structure all cations are in sixfold coordination, in the

B-type structure some of them are surrounded by seven oxygen anions. This sevenfold coordination is a characteristic feature of the A-type structure. Both the H- and X-type structures are built from octahedral, which are distorted in the former case.

Yb_2O_3 has a cubic structure below 1870 °C and is used as a catalyst in the petrochemical industry [6]. At higher temperatures it exists in both monoclinic and hexagonal phases [7]. The crystal structure of the Yb_2O_3 is well known. The oxide crystallizes in the bixbyite structure in the space group Ia-3. In this space group, cations occupy the special positions $8b$ and $24d$ [8] with local symmetries C_{3i} and C_2, respectively. The position $24d$ has one degree of freedom. The cations in both positions are octahedrally surrounded by oxygen ions. The oxygen ion in the general $48e$ position is surrounded by four cations [8]. Cation site occupancy is a very important structural parameter that determines optical, magnetic and the other physical properties. RE^{3+} ions in the host sesquioxide matrices are preferable in the C_2 site from an optical point of view [9].

The Yb_2O_3 is of special interest due to the presence of Yb^{3+} ions, which are the last in the lanthanide series with unfilled f shells. The free Yb^{3+} ion has the configuration $4f^{13}$ which gives rise to a $J=7/2$ ground manifold and a $J=5/2$ excited manifold at about 10 000 cm^{-1}. Of the splitting of all of the rare-earth ions, these splitting for Yb^{3+} are the largest, and hence the excited manifold $J=5/2$ does not significantly contribute to the magnetic properties. Because of the simple energy level diagram of Yb^{3+}

* Corresponding author. Fax: + 216 71 573526.
E-mail address: rached.benhassen@fss.rnu.tn (R. Ben Hassen).

ion in the crystal field and its pronounced optical activity, it is considered as a good candidate to replace Nd^{3+} in laser materials [10,11].

In the RE–RE^1 binary mixed oxides at a fixed temperature, the crystalline type depends on the structures of RE_2O_3 and $RE^1_2O_3$ and on the difference between their cation radii as well [12]. If the single RE sesquioxides possess the same structure, a solid solution forms which follows Vegard's law. On the contrary, the oxides which do not crystallize in the same structure type, give rise to two terminal solid solutions with the structures of the two pure oxides and to one or more polyphasic regions, where A and B or B and C types can coexist [13]. If the difference among the ionic radii is large enough to satisfy the Goldschmidt tolerance factor, a distorted perovskitic compound forms [14] for the equimolar composition.

In our previous works [15–18], we tried to delineate the phases present in some Re–T binary mixed oxides ($RE=$Yb, Lu and $T=$Ni, Co) system using powder XRD and Raman spectroscopic techniques. It has been demonstrated clearly that Yb_2O_3–CoO and Yb_2O_3–NiO systems show single phasic C-type phase field near the pure Yb_2O_3 and then enter the biphasic phase field for upper transition element contents. The cationic distribution over the two non-equivalent sites 8b and 24d of the space group is found to be random for all composition. The Raman results point towards a tetrahedral coordination of the Co^{3+} (Ni^{3+}) cations in the $Yb_{2-x}Co_xO_3$ ($Yb_{2-x}Ni_xO_3$) series. It was also found that Co^{3+} ions strongly prefer to enter the Lu_2O_3 host at the C_2 site. The solubility of Co in the Lu_2O_3 host was found to be limited. The existence of Ni^{2+}/Co^{3+} ions in $Yb_{2-x}Ni_xO_3/Yb_{2-x}Co_xO_3$ has no future on the magnetic ordering.

In the present work, we intend to extend this study with the Yb_2O_3–Cr_2O_3 system. The method used for synthesizing $Yb_{2-x}Cr_xO_3$ and the powder X-ray diffraction results of the compounds including unit-cells information magnetic measurements and diffraction data are reported.

In doped rare-earth sesquioxide, lattice parameters and other physical properties of the samples tend to change with composition and are an interesting interplay of relative sizes of doping cation and RE^{3+} as well as the oxygen vacancies created as the result of a potential aliovalent substitution [19]. Also, this may lead to the stabilization of high-temperature phases of rare earths at ambient temperature. This makes the study of phase evolution in rare-earth doped chromium an interesting research area. However, X-ray diffraction technique is found to be insensitive to microscopic phase changes initiated by oxygen displacement, because X-ray scattering efficiency of oxygen is significantly lower as compared to that of the high Z rare-earth cations. Moreover, owing to large coherence length of X-rays, it is not often easy to detect parasitic micro domains of altogether different new phases amidst a bulk phase using XRD technique [20]. Raman spectroscopy becomes useful in such cases and promise better results because of its sensitivity to both oxygen displacement due to large polarizability [21] and intermediate range order without long range periodicity [2,22].

2. Experimental

The polycrystalline samples of $Yb_{2-x}Cr_xO_3$ ($x=0.01$, 0.02, 0.03, 0.04, 0.05 and 0.1) are prepared by using a water-soluble complex method as reported elsewhere [18]. For representative phase with $x=0.03$, an excess of citric acid (Riedel-de-Han, 99.5%) in granular form mixed together with appropriate proportions of ytterbium oxide (Aldrich, 99.9%) and chromium nitrate nanohydrate (Aldrich, 99.9%) corresponding to the stoichiometry of the $Yb_{2-x}Cr_xO_3$ were introduced with magnetic stirring into 50 ml

of 6 M nitric acid solution. The whole mixture was then stirred at 60–80 °C until the solution became completely transparent, containing metal ion and citric acid complexes. The transparent solution was further heated at 90 °C overnight with excess solvent to promote polymerization. During the continuous heating, the solution became more viscous with a change of colour from greenish blue to brown, but without any visible formation of precipitation or turbidity. A portion of the resin in a porcelain crucible was pyrolized at 200–350 °C for 2 h in an electrical furnace (Carbolite), resulting in solid mass, which was lightly ground into a black powder. The crystalline $Yb_{2-x}Cr_xO_3$ was obtained by the calcination of the obtained powder precursor at 1000 °C for 12 h. Powder X-ray data were collected at room temperature using a Philips PW1730 diffractometer with Cu $K\alpha$ radiation. The data collection conditions were 10–100° 2θ in 0.02° steps, with integration times of 30 s. The X-ray powder diffraction data were refined by the Rietveld method [23] for crystal structure using the FULLPROF program and a refined background function [24].

The Fourier-transformed infrared FT-IR spectra were recorded with a FT-IR spectrometer operated in transmission mode. Prior to analysis, each sample was diluted in IR-grade potassium bromide (5%) by weight and pressed into self-supported discs 13 mm in diameter and approximately 100 mg in weight.

The Raman spectra were recorded at room temperature with the 647.1 nm excitation line from a Spectra Physics krypton ion laser. The compounds were studied with a very low laser power (3 mW the sample). Four accumulations of few seconds have been used for each spectral range. No damage of the material by the laser has been observed. The beam was focused onto the samples using the macroscopic configuration of the apparatus.

The magnetic measurements in the temperature range of 2–100 K were performed with a Foner magnetometer (FON). Magnetization of the sample was measured in an isothermal regime under an applied magnetic field varying from 0 to 10 T.

3. Results and discussion

The XRD patterns of all the products in $Yb_{2-x}Cr_xO_3$ series were recorded and analysed. They are shown in Fig. 1. The parent compounds Cr_2O_3 is rhombohedral (R-$3c$) whereas Yb_2O_3 is C-type cubic (Ia-3). Two defined compounds $YbCrO_3$ (JCPDS # 25-51076) orthorhombic ($Pbnm$) and $YbCrO_4$ [25] tetragonal ($I41/amd$) are already known for this binary system. It was observed when
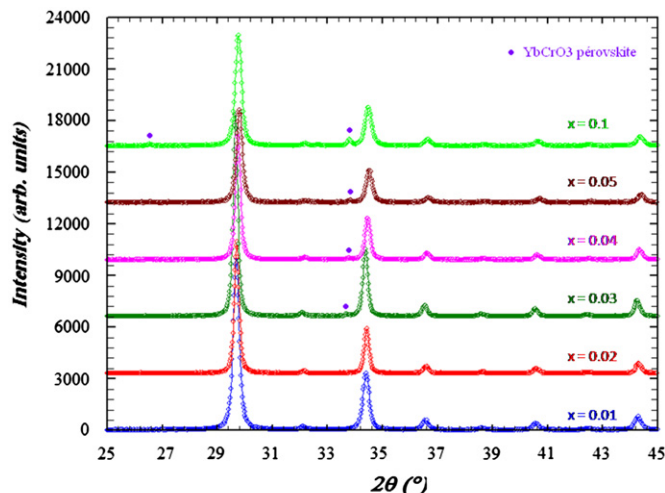
Fig. 1. X-ray diffraction of the system ($Yb_{2-x}Cr_xO_3$) for different composition.

analysing the recorded patterns (Fig. 1) that on doping 2 mol% Cr into Yb_2O_3; the XRD pattern consisted of peaks due to C-type sesquioxide lattice. This implies that the 2 mol% Cr is soluble in Yb_2O_3 and hence this nominal composition is monophasic C-type. On increasing the concentration of Cr to 3 mol%, peaks corresponding to perovskite $YbCrO_3$ appeared. Hence, the prepared powder with initial composition corresponding to $x=0.03$ is biphasic consisting of both C-type phase sesquioxide and the perovskite structure of $YbCrO_3$. This trend was continued till 10 mol%. Starting from $x=0.01$–0.03, the C-type peaks were found to shift towards higher angle with increase in amount of Chrome thereby further indicating the solubility of Cr into Yb_2O_3. The intensities of peaks corresponding to the $YbCrO_3$ phase increase with the initial composition of Cr.

An important implication of this result that is the limit of Cr solubility in Yb_2O_3 is about 2.8 mol%. Thus the wider range of biphasicity and lesser solubility observed in Yb_2O_3–Cr_2O_3 series as compared to Yb_2O_3–Y_2O_3 [26] can be attributed to larger difference in ionic sizes of Yb^{3+} and Cr^{3+} as compared to that between Yb^{3+} and Y^{3+} which affects their miscibility behaviour.

Rietveld refinements were performed for diffraction data sets of samples with initial compositions $x=0.01$, 0.02, 0.03 in the space group $Ia-3$. For samples with initial compositions $x>0.03$, a biphasic Rietveld refinements were applied. The starting structure parameters for the refinement process were taken from Yb_2O_3 and $YbCrO_3$ [27]. The profiles of reflections were described by using the pseudo-Voigt function. The correction for background is made by, first selecting background points and then a correction algorithm. Winplotr program was used for these tasks [24]. For solid solutions $Yb_{2-x}Cr_xO_3$ which form the majority phase in all samples treated, the atomic parameters were: three fractional coordinates for oxygen ions, x-coordinate for ions in 24d position, two isotropic temperature B factors of 24d and 8b positions and occupation number for Cr^{3+} ion in 24d position. This occupation number was coupled with occupation number of Cr^{3+} ion in 8b position in order to keep appropriate stoichiometric ratio. Thermal displacement factors of oxygen atoms are not refined and fixed to values bigger than those of heavy atoms. In Rietveld refinements of heavy-atom structures much problematic intensity may be hidden in the thermal displacement factors of relatively light atoms. Fig. 2 shows the results of the refinement for the composition $x=0.03$. The results obtained for the final lattice parameters, positional coordinates and atomic occupancies are given in Table 1.
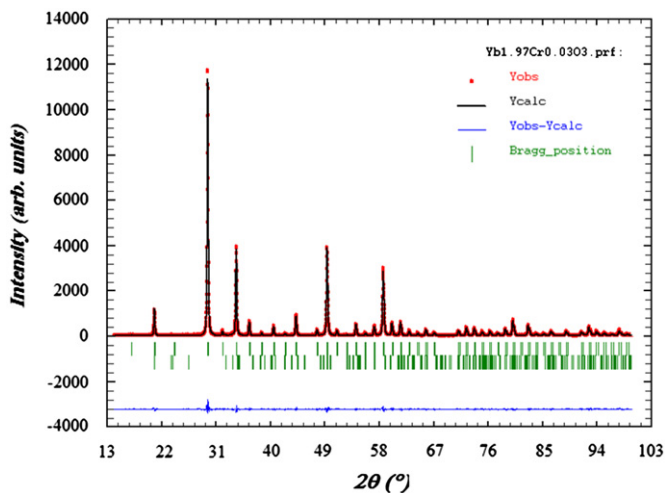
Table 1
Refined values of the atomic parameters for $Yb_{2-x}Cr_xO_3$.

Composition x	$x=0.01$	$x=0.02$	$x=0.03$
a (Å)	10.4402(4)	10.4388(2)	10.4372(1)
(Yb/Cr) 24d x	0.9683(1)	0.9678(1)	0.9677(5)
O x	0.3904(10)	0.3902(12)	0.3920(6)
O y	0.1542(8)	0.1545(11)	0.1531(5)
O z	0.3764(11)	0.3803(13)	0.3806(6)
Occ (Yb 8b)	0.1645(13)	0.164(1)	0.163(1)
Occ (Cr 8b)	0.0021(13)	0.002(1)	0.003(1)
Occ (Yb 24d)	0.4971(11)	0.495(2)	0.493(4)
Occ (Cr 24d)	0.0029(11)	0.005(2)	0.007(4)
B_{iso} (Yb/Cr 8b) (Å^2)	1.98(8)	1.67(6)	1.71(4)
B_{iso} (Yb/Cr 24d) (Å^2)	2.06(2)	1.69(6)	1.71(3)
R_B (%)	2.91	3.35	1.36
R_P (%)	11.5	13.4	7.41
R_{WP}(%)	15.1	19.7	10.5
R_{exp}(%)	9.24	15.8	9.38
χ^2	2.66	1.56	1.25
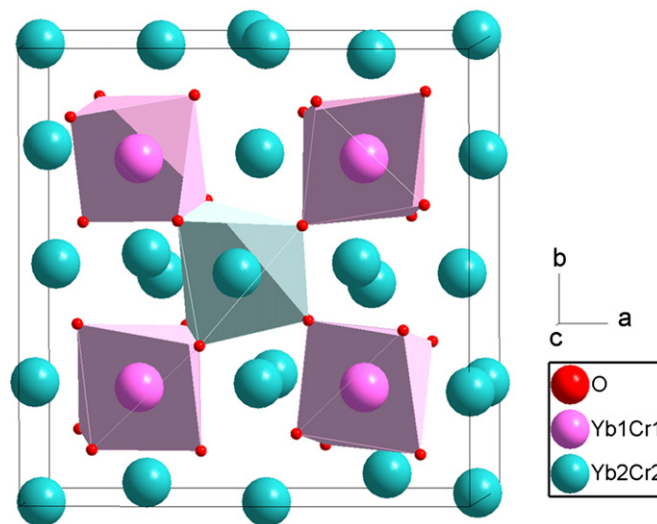
Fig. 3. Oxygen octahedra in the cubic rare-earth bixbyite structure. For clarity, only one half of the unit cell is shown.

The structure of the solid solution $Yb_{2-x}Cr_xO_3$ is built of two layers: the first consist of distorted $(Yb/Cr)O_6$ octahedral around the 24d and 8b positions, while the second consists exclusively of distorted octahedral around 24d positions. Fig. 3 shows the unit cell with the oxygen octahedral around the 24d and 8b positions.

From these tabulated results one can observe that for samples with initial compositions $x \leq 0.03$, replacing Yb^{3+} by Cr^{3+} decreases the lattice parameter a, which can be attributed to the larger radius of Yb^{3+} ion compared with the Cr^{3+} ion. The B-factors are similar for cations in the two-crystallographic position (Table 1).

As shown in Fig. 4, the lattice parameter a decreases with the increase of the Cr concentration x is nearly linear and obeying Vegard's rule

$$a(\text{Å}) = a_0 + a_1 \times x$$

where the parameter of the linear fitted to the data are $a_0=10.441$ Å corresponds to Yb_2O_3 [28] and $a_1=-0.1137$ Å corresponds to the difference of the ionic radii r (Yb^{3+})=0.858 Å [29] and r (Cr^{3+})=0.615 Å [30]. This slight deviation from linearity may be attributed to some impurity in the precursor materials or some errors during the weighting. The site occupancies of the cations Yb^{3+} and Cr^{3+} in the two sites 8b and 24d were

Fig. 2. Part of the diffraction pattern fitting of $(Yb_{1.97}Cr_{0.03})O_3$ resulting from Rietveld refinement.
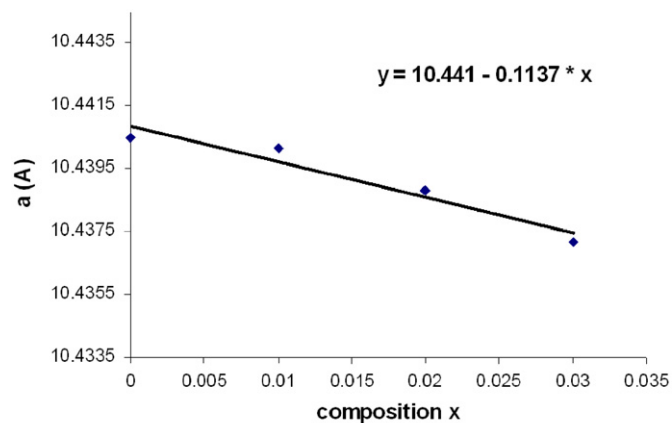
Fig. 4. Variation of the lattice parameter a for the system $Yb_{2-x}Cr_xO_3$ with compositions.

Table 2
Selected bond lengths (Å) for the refined phases.

Composition x	$x=0.01$	$x=0.02$	$x=0.03$
Yb/Cr (8b)[1]–O (Å)	2.21(1)	2.23(1)	2.25(6)
Yb/Cr(24d)[2]–O (Å)	2.22(1)	2.19(1)	2.19(6)
	2.23(1)	2.26(1)	2.24(6)
	2.33(1)	2.30(1)	2.31(6)

coupled and refined keeping the overall occupancy of the respective sites constant according to the appropriate stoichiometric ratio. The occupancies of oxygen ions were not refined and were fixed for all refinements. To check the cation ordering in the two non-equivalent sites of the structure (X-ray diffraction is not sensitive enough), the coefficients of the cationic distribution K is calculated from the equation

$$K = \frac{OccYb(8b)xOccCr(24d)}{OccCr(8b)xOccYb(24d)}$$

where OccYb (8b)/(24d) and OccCr (8b)/(24d) are the occupancies of Yb^{3+} and Cr^{3+} ions at 8b and 24d positions, respectively. If K is equal or close to 1, a random distribution is present. The obtained K values are 0.457, 0.828 and 0.771 for the samples with $x=0.01$, 0.02 and 0.03, respectively. The values of the coefficient K show in all of the samples a strong manifestation of preferential cationic distribution. The preferential distribution can be explained by the big radii difference. In fact the host ions Yb^{3+} are of bigger radius than the doped ones Cr^{3+} and random distribution is easily obtained. Similar behaviour was already observed in literature with Eu^{3+} in $Y_{2-x}Eu_xO_3$ [31], Yb^{3+} in $Y_{2-x}Yb_xO_3$ [26], Dy^{3+} in $Y_{2-x}Dy_xO_3$ [32] and Gd^{3+} in $Er_{2-x}Gd_xO_3$ [33], which is attributed in the last case to the small difference in ionic radii of Er^{3+} and Gd^{3+}. Nevertheless, the cationic distribution, preferential or random, greatly depends on the preparation method [33].

The variation of the bond lengths of the oxygen octahedral with the composition x is shown in Table 2. The oxygen ions are equidistant for cations in 8b positions, but the angles deviate from 90°. Around the 24d positions the oxygen ions are distributed in the conformation two+two+two at three distances (Fig. 5). From Table 2 we can see systematic variation in the bond lengths of $(Yb/Cr)O_6$ octahedral around 8b and 24d as x varies from 0.01 to 0.03. These changes of the bond lengths may be ascribed to the preferential distribution of Cr^{3+} ion.

For samples with initial compositions $x > 0.03$, we noted a change in behaviour for the a parameter and the appearance of
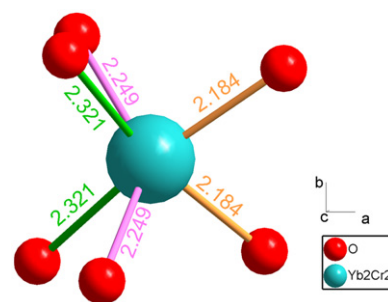
Fig. 5. Octahedral environment of the 24d cation for $x=0.03$.
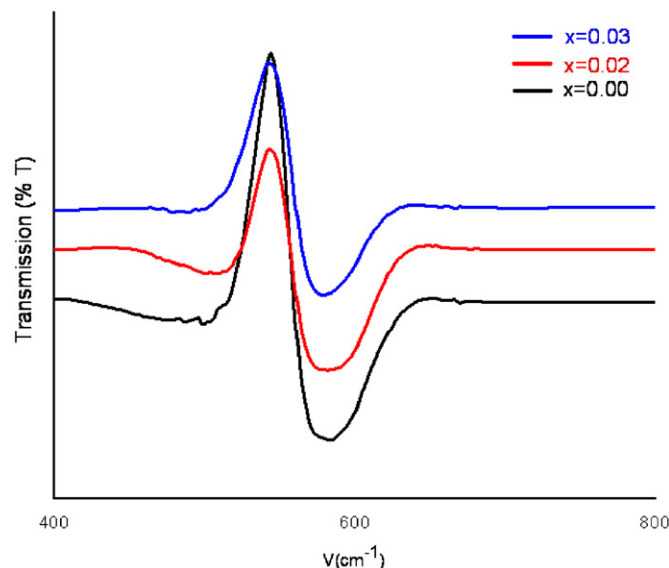
Fig. 6. IR spectra from $Yb_{2-x}Cr_xO_3$.

peaks associated to $YbCrO_3$ phase in the X-ray diffraction patterns (Fig. 2). This trend indicates that the solid solution solubility limit is reached and was approximately evaluated at 2.8 mol% Cr by using a Rietveld refinement.

We tried to present only the Infrared spectra for $Yb_{2-x}Cr_xO_3$ series with $x < 0.03$ in comparison with the spectrum of Yb_2O_3 in Fig. 6. Our spectrum of Yb_2O_3 agrees to within a few cm^{-1} with the data of White and Keramidas [34]. The spectral signature of each of these compounds is representative of the C-type cubic sesquioxide structure. In Cr_2O_3, the sharp bands at 640 and 440 cm^{-1} are assigned to Cr–O stretching and the O–Cr–O deformation vibration [35]. In Yb_2O_3, the sharp band at 589 cm^{-1} is assigned to Yb–O stretching vibrations. The position of the Yb–O as well as the Cr–O band does not change significantly when increasing the extent of chromium doping. The strongest bands in the spectrum occur near 400 cm^{-1} and usually appear as broad. The positions of the Yb–O and Cr–O bands are very close and overlapped and it seems very difficult to give detailed assignment to the observed spectra. Below the broad absorption a sharp bands that appear rather consistently through all spectra.

To further study the doping effect on the structure by the replacement of Yb^{3+} ions with Cr^{3+}, Raman spectroscopy of $Yb_{2-x}Cr_xO_3$ $(0 < x \leq 0.05)$ only was performed with 514.5 nm excitation light.

Fig. 7 shows the normalized Raman spectra of all considered samples, recorded at room temperature. It can be seen that the characteristic Raman peaks of Yb_2O_3 laying at 307, 342, 365, 428 and 461 cm^{-1} are in good agreement with those reported in the
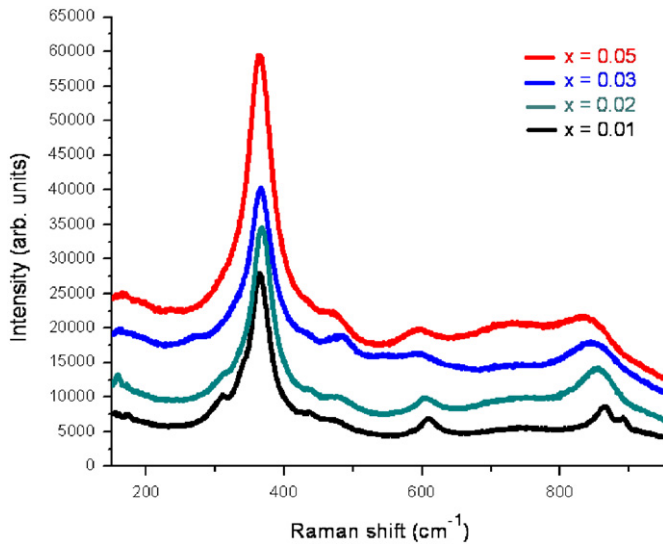
Fig. 7. Raman spectra from $Yb_{2-x}Cr_xO_3$.
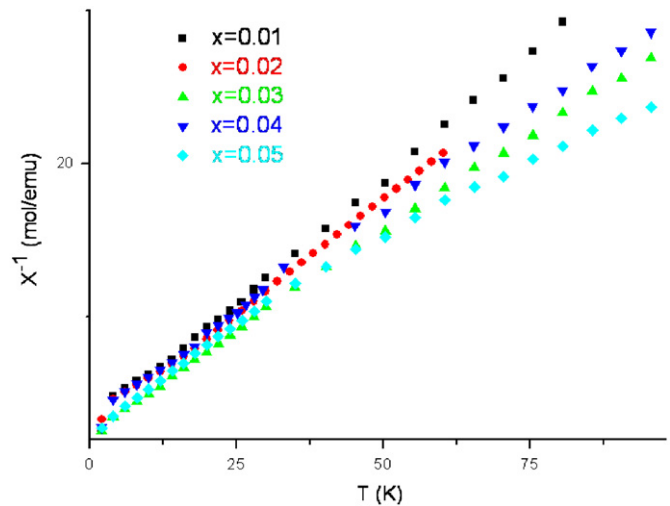
Fig. 8. The inverse low temperature susceptibilities for $Yb_{2-x}Cr_xO_3$ samples.

literature [36]. The strong Raman intensity measured for the band at $365\ cm^{-1}$ indicates a large polarizability change during the vibration [37]. Therefore this band is expected to be more sensitive to change in chemical bonding.

Raman spectra presented in this work are, in general, in good agreement with the literature [37–39]. First of all, it should be noted that none of the spectra shows the expected number of bands. It has previously been shown by White and Keramidas [34] that factor group theory predicts the $4A_g(Raman)+4E_g(Raman)+5A_u(inactive)+16T_u(IR)$ modes for this type of structure.

In many cases, some bands are quite large. Therefore, some of them are likely overlapped, at least partially. A similar behaviour was reported in our previous works [15–18] and even in Raman spectra of single crystals of Sm_2O_3 [38] or Y_2O_3 [40] even collected at 5 K. It could be possible that local stress and a large number of point defects can lead to a local lowering of symmetry and to the band broadening [41]. In case of powders, the crystallinity can be lower and these effects might be even greater.

The Cr-doping did not change the C-type structure of the material. However, the relative intensity of Raman peak at $307\ cm^{-1}$ decreased and vanished for the composition $x=0.03$. The vibration modes observed around 870 and $890\ cm^{-1}$ are associated with different Cr–O vibrations in the octahedron CrO_6. By increasing the Cr concentration, we see the merging of these two peaks to form a broad band which shifts to lower frequencies, indicating the increase of the lattice distortion with Cr^{3+} doping. This lattice distortion may mainly be caused by the difference of ionic radii between Cr^{3+} and Yb^{3+} and consequently, the deformation of chromium oxygen polyhedra which weakens the Cr–O covalent linkage.

The observed temperature dependencies of the inverse susceptibilities for different concentrations x are depicted in Fig. 8. The least square fit to the modified Curie–Weiss law shows paramagnetic interaction in $Yb_{2-x}Cr_xO_3$ ($0<x\leq0.05$) for all the measured concentrations. The $YbCrO_3$ phase impurity will have no influence on the magnetic properties of the samples in fact, a nearly temperature independent paramagnetism was observed at low temperatures.

The temperature dependencies of the inverse molar paramagnetic susceptibility of $Yb_{2-x}Cr_xO_3$ ($0<x\leq0.05$) samples can be divided into two regions. In the low-temperature region, for $T<37$ K, the inverse paramagnetic susceptibilities depend linearly on temperature (Fig. 8). However, in the high-temperature

region, for $T>37$ K, the inverse paramagnetic susceptibilities are non-linear versus temperature (Fig. 8). This deviation from the Curie–Weiss behaviour reflects the splitting of the Yb^{3+}-ion ground state under the influence of the crystal field. In the crystal fields of C_2 and C_{3i} symmetry, corresponding to the crystallographic positions 24d and 8b, respectively, the eightfold ground level $^2F_{2/7}$ of Yb^{3+} ions splits into four Kramer's doublet [31]. The values of the effective magnetic quantum number of each sublevel should be obtained as a linear combination of the magnetic quantum numbers of the free ion.

In the low temperature range ($T<37$ K) only the lowest Kramer's doublet of Yb^{3+} ions is populated [31], and the effective magnetic moment corresponds to this doublet. Consequently, in this region, the paramagnetic susceptibilities can be fitted to a modified Curie–Weiss law

$$\chi_M = \frac{C_M}{T-\theta} + \chi_0$$

where C_M denotes the molar Curie constant $C_M=(2-x)(N_{Av}g_J^2\mu_B^2\mu_{eff}^2/3k_B)$, where x denotes the concentration, N_{Av} is Avogadro's number, $g_J=8/7$ is Lande's splitting factor, μ_B is the Bohr magneton, μ_{eff} is the effective magnetic quantum number of the lowest Kramer's doublet of Yb^{3+} ions, k_B is the Boltzmann constant and θ is the Curie–Weiss paramagnetic temperature. Curie constants $C_M(x)$ are determined from the slopes of the lines $\chi_M=f(T)$ and are respectively 4.37, 3.93 and 2.99 emu K/mol for $x=0.01$, 0.02 and 0.03. $C_M(0)$ gives effective magnetic moments of Yb^{3+} ion in the Yb_2O_3 $\mu_{eff}=4.03\ \mu_B$ (Fig. 9), close to its free-ion value 4 μ_B. The fact, that all μ_{eff} values of Yb^{3+} in $Yb_{2-x}Cr_xO_3$ are smaller than free ions value, points to the crystal field influence.

4. Conclusions

The present study clearly delineates the phases present in $Yb_2O_3–Cr_2O_3$ system and it has been demonstrated clearly using powder XRD and Raman spectroscopic technique. $Yb_2O_3–Cr_2O_3$ system shows single phasic C-type phase field up to 2.8 mol% and then enters the biphasic phase field. The cationic distribution over the two non-equivalent sites 8b and 24d of the space group $Ia-3$ was found to be random for all composition. The Raman spectroscopy reveals the increase of the lattice distortion with Cr^{3+} doping. This lattice distortion may mainly be caused by the difference of ionic radii between Cr^{3+} and Yb^{3+}. The modified Curie–Weiss law shows paramagnetic interaction in $Yb_{2-x}Cr_xO_3$
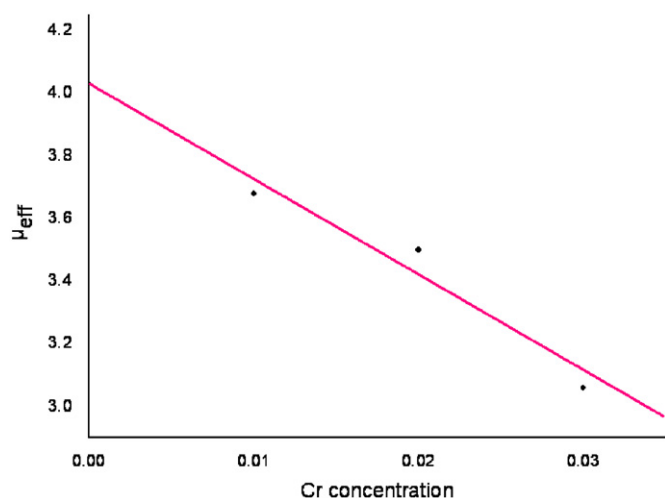
Fig. 9. Evolution of the effective magnetic moment with the Chrome concentration.

$(0 < x \leq 0.03)$. In the region 2–37 K only the lowest Kramer's doublet is populated, and for that level the effective magnetic quantum number is deduced.

References

[1] Y. Maki, M. Matsuda, T. Kudo, Solid Electrolyte Fuel Cell, U. S. Patent 3 (607) (1971) pp. 424.
[2] M. Yahshima, H. Arashi, M. Kakihana, M. Yoshimura, J. Am. Ceram. Soc. 77 (1994) 1067–1071.
[3] Y.S. Zheng, K.M. Knowles, J.M. Vieira, A.B. Lopes, F.J. Oliveira, J. Microsc. 201 (2001) 238–249.
[4] G. Brauer, in: L. Eyring (Ed.), Progress in the Science and Technology of the Rare Earths, Pergamon Press, Oxford, 1968, pp. 434–457.
[5] R.G. Haire, L. Eyring., in: K.A. Gschneidner Jr., L. Eyring, G.R. Choppin, G.H. Lander (Eds.), Handbook on the Physics and Chemistry of Rare Earths, Vol. 18, Elsevier, New York, 1994, pp. 413–505.
[6] H. Arakawa, Technol. Jpn. 21 (11) (1988) 32.
[7] P. Kofstad, Nonstoichiometry Diffusion and Electrical Conductivity in Binary Metal Oxides, Wiley-Interscience, New York, 1972.
[8] M. Marezio, Acta Cryst. 20 (1966) 723–728.
[9] G. Concas, G. Spano, E. Zych, J. Trojan-Piegza, J. Phys. Condens. Matter 17 (2005) 2597–2604.
[10] L. Laversenne, Y. Guyot, C. Goutaudier, M.Th. Cohen-Adad, G. Boulon, Opt. Mater. 16 (2001) 475–483.
[11] J.H. Mun, A. Novoselov, A. Yoshikawa, G. Boulon, T. Fukuda, Mater. Res. Bull. 40 (2005) 1235–1243.
[12] M. Marezio, Acta Crystall. 20 (1966) 723–728.
[13] P. Mele, C. Artini, A. Ubaldini, G.A. Costa, M.M. Carnasciali, R. Masini, J. Phys. Chem. Solids 70 (2009) 276–280.
[14] M. Zinkevich, Prog. Mater. Sci. 52 (2007) 597–647.
[15] L. Ben Farhat, M. Amami, E.K. Hlil, R. Ben Hassen, J. Alloys Comps. 485 (2009) 701–705.
[16] L. Ben Farhat, M. Amami, E.K. Hlil, R. Ben Hassen, Mater. Res. B 45 (2010) 1964–1968.
[17] L. Ben Farhat, M. Amami, E.K. Hlil, R. Ben Hassen, Mater. Chem. Phys. 123 (2010) 737–741.
[18] L. Ben Farhat, M. Amami, E.K. Hlil, R. Ben Hassen, J. Alloys Compd. 479 (2009) 594–598.
[19] V. Grover, A.K. Tyagi, Mater. Res. B 39 (2004) 859–866.
[20] A. Nakajima, A. Yoshihara, M. Ishigame, Phys. Rev. B 50 (1994) 13297–13307.
[21] C. Kittel, Introduction to Solid State Physics, fourth Ed., Wiley, New York, 1971.
[22] B.P. Mandal, V. Grover, M. Roy, A.K. Tyagi, J. Am. Ceram. Soc. 90 (2007) 2961–2965.
[23] H. Rietveld, J. Appl. Crystallogr. 2 (1969) 65–71.
[24] T. Roisnel, J. Rodriguer-Carvajal, Mater. Sci. Forum 378–381 (2001) 118–123.
[25] E.V. Leutkina, N.A. Puretskii, A.P. Bobylev, L.N. Komissarova, Theor. Found. Chem. Eng. 41 (2007) 567–571.
[26] M. Mitric, B. Antic, M. Balanda, D. Rodic, M.Lj. Napijalo, J. Phys.: Condens. Matter 9 (1997) 4103–4111.
[27] G. Will, Aust. J. Phys. 41 (2) (1988) 293–296.
[28] Z.K. Heiba, J. Appl. Crystallogr. 38 (2005) 306–310.
[29] R.D. Shannon, C.T. Prewitt, Acta Cryst. B 25 (1969) 925–946.
[30] Katherine L. Crispin, James A. Van Orman, Phys. Earth Planet. Inter. 180 (2010) 159–171.
[31] B. Antic, M. Mitric, D. Rodic, J. Phys. Condens. Matter 9 (1997) 365–374.
[32] B. Antic, P. Onnerud, D. Rodic, R. Tellgren, Powder Diffr. 8 (1993) 216–219.
[33] Z.K. Heiba, Y. Akin, W. Sigmund, Y.S. Hascicek, J. Appl. Crysallogr. 36 (2003) 1411–1416.
[34] W.B. White, V.G. Keramidas, Spectrochim. Acta 28A (1972) 501–509.
[35] G.V. Subba Rao, C.N.R. Rao, J.R. Ferraro, Appl. Spectrosc. 24 (1970) 436–445.
[36] N. Dilawar, S. Mehrotra, D. Varandani, B.V. Kumaraswamy, S.K. Haldar, A.K. Bandyopadhyay, Mater. Charact. 59 (2008) 462–467.
[37] A. Ubaldini, M.M. Carnasciali, J. Alloys Compd. 454 (2008) 374–378.
[38] Y. Repelin, C. Proust, E. Husson, J.M. Beny, J. Solid State Chem. 118 (1995) 163–169.
[39] J.C. Panitz, J.C. Mayor, B. Grob, W. Durisch, J. Alloys Compd. 303/304 (2000) 340–344.
[40] J.F. Martel, S. Jandl, A.M. Lejus, B. Viana, D.J. Vivien, J. Alloys Compd. 353 (1998) 275–277.
[41] J.M. Calderon-Moreno, M. Yoshimura, Solid State Ionics 154/155 (2002) 125–133.